RESEARCH ARTICLE

NANO · MICRO small
www.small-journal.com

A Mixed-Pure Planar Heterojunction Structure of Active Layers for Efficient Sequential Blade-Coating Organic Solar Cells

Yilin Wang, Yabing Tang, Yanni Ouyang, Weiwei Wu, Acacia Patterson, Obaid Alqahtani, Tanner Melody, Ke Zhou, Guanghao Lu, Jie Min, Chunfeng Zhang, Han Yan, Qunping Fan, Long Jiang,* Brian A. Collins,* and Wei Ma**

Precise modulating the vertical structure of active layers to boost charge transfer is an effective way to achieve high power conversion efficiencies (PCEs) in organic solar cells (OSCs). Herein, efficient OSCs with a well-controlled vertical structure are realized by a rapid film-forming method combining low boiling point solvent and the sequential blade-coating (SBC) technology. The results of grazing incident wide-angle X-ray scattering measurement show that the vertical component distribution is varied by changing the processing solvent. Novel characterization technique such as tilt resonant soft X-ray scattering is used to test the vertical structure of the films, demonstrating the dichloromethane (DCM)-processed film is truly planar heterojunction. The devices with chloroform (CF) processed upper layer show an increased mixed phase region compared to these devices with toluene (TL) or -DCM-, which is beneficial for improving charge generation and achieving a superior PCE of 17.36%. Despite significant morphological varies, the DCM-processed devices perform slightly lower PCE of 16.66%, which is the highest value in truly planar heterojunction devices, demonstrating higher morphological tolerance. This work proposes a solvent-regulating method to optimize the vertical structure of active layers through SBC technology, and provides a practical guidance for the optimization of the active-layer microstructure.

1. Introduction

Organic solar cells (OSCs) have a bright prospect among academic and industrial communities due to their unique features such as lightweight, low cost, semitransparent properties, and large-area printing compatibility.[1–5] It is well established that, the microstructure of bulk heterojunction (BHJ) active layer is closely associated with the power conversion efficiencies (PCEs) of OSCs.[6–13] The morphological parameters of active layers, such as crystallization, molecular orientation, phase separation size, and purity are important factors that affect the exciton dissociation, charge extraction, and transfer properties of OSCs.[14–19] Up to now, most of the active layer optimization methods focus on the transverse morphology (also known as lateral morphology) to study the aforementioned morphological parameters, which are basically skillful and well characterized.[20,21] Therefore, the ideal

Y. Wang, Y. Tang, K. Zhou, H. Yan, Q. Fan, W. Ma
State Key Laboratory for Mechanical Behavior of Materials
Xi'an Jiaotong University
Xi'an 710049, China
E-mail: qunping@xjtu.edu.cn; msewma@xjtu.edu.cn

Y. Ouyang, C. Zhang
National Laboratory of Solid State Microstructures
School of Physics
and Collaborative Innovation Center for Advanced Microstructures
Nanjing University
Nanjing 210093, China

W. Wu, J. Min
The Institute for Advanced Studies
Wuhan University
Wuhan 430072, China

A. Patterson, O. Alqahtani, T. Melody, B. A. Collins
Department of Physics and Astronomy
Washington State University
Pullman, WA 99164, USA
E-mail: brian.collins@wsu.edu

O. Alqahtani
Department of Physics
Prince Sattam bin Abdulaziz University
Alkharj 11942, Kingdom of Saudi Arabia

G. Lu
Frontier Institute of Science and Technology
Xi'an Jiaotong University
Xi'an 710054, China

L. Jiang
State Key Laboratory of Oil and Gas Equipment
CNPC Tubular Goods Research Institute
Xi'an, Shaanxi 710077, China
E-mail: jianglong003@cnpc.com.cn

The ORCID identification number(s) for the author(s) of this article can be found under https://doi.org/10.1002/smll.202407435

DOI: 10.1002/smll.202407435

transverse structure is determined and have a large amount of research work available for reference. However, the deep understanding of the active layer vertical structure is still unclear due to some difficulties, such as the vertical thickness of the restricted domain (normally, the optimal active layer thickness is ≈100 nm) and the complexity of data resolution.[22,23] On the other hand, single solvent processing of BHJ structure has been the main method for preparing active layers.[1,12] Due to the partial miscibility of components, the internal morphology of active layer is complicated, which directly affects the charge separation and transport processes of OSCs.[23] Moreover, the unsatisfactory distribution of these phase regions in the vertical direction can also hinder the charge separation and transport processes of OSCs.[23] The above problems make it difficult to study the vertical structure of the BHJ active layers, which undoubtedly hinders the OSCs from further improving PCEs.[24] Therefore, optimizing the vertical morphology has become the study focus and breakthrough in the preparation of high-quality active layers.[25,26] Therefore, how to precisely regulate the active layer morphologies with the most favorable vertical structure for boosting the charge separation and transport processes is the key to promote the PCEs of OSCs.

Recently, preparing the P-i-N structures by sequential deposition of components has become a normally used method to modulate the vertical structure of active layers, leading to a more favorable nanostructures as compared to BHJ morphology.[4,27] First, the donor and acceptor components can be independently optimized, eliminating the mutual influence of phase separation and crystallization among each component in the complex film-formation kinetics process.[23,27] Then, the stratified deposition of donor and acceptor components is more conducive to the formation of ideal vertical phase separation and effectively reduces bimolecular recombination of related OSCs.[28–31] Therefore, sequential processing is expected to alleviate the device performance loss caused by film morphology defects. Meanwhile, the film-forming conditions such as processing solvent, film-forming speed, annealing temperature, and time, have an important effect on the vertical structure of active layers.[32] For the photovoltaic performance of OSCs, the evolution process of active layer materials from solution to film is crucial. For example, molecular aggregation state in solution, solvent evaporation rate, and other characteristics will significantly affect the processes of crystallization nucleation and crystal growth of photovoltaic materials, so as to directly regulate the final active layer morphology.[33–36] To prepare the high-quality films, active layers, their film formation time should be carefully controlled, which is greatly affected by processing solvent.[37] Due to the variable boiling points and material solubility of different solvents, the related morphology of the vertical component distribution can be well manipulate by changing the processing solvent of the upper layer during the sequential deposition.[28] Therefore, the vertical structure of active layers can be regulated effectively by selecting solvent with different boiling points to control the film formation rate and time. However, there is limited systematic studies and the related working mechanism is still unclear.

Herein, we developed highly efficient P-i-N structured OSCs in an ambient condition with a well-controlled vertical structure of active layers by combining the rapid film-forming method and the sequential blade-coating (SBC) strategy. The polymer donor D18 was first dissolved in chloroform (CF) and deposited on the substrate, then YSe acceptor was dissolved in toluene (TL), CF, or dichloromethane (DCM) and coated on the D18 upper layer separately, of which the boiling point of solvents gradually decreased, to prepare the active layers of OSCs corresponding to SBC-TL, SBC-CF, and SBC-DCM, respectively. Among them, the SBC-CF OSCs exhibited a superior PCE of 17.36% mainly due to their favorable morphology. In the ex situ and in situ measurements, the SBC-CF film showed an enhanced crystallinity of acceptor and increased mixed phase region, which are beneficial for improving charge transport and decreasing bimolecular recombination of OSCs. Interestingly, the SBC-DCM OSCs offered a similar but slightly lower PCE of 16.66% compared with the SBC-CF ones. Therefore, vertical structures of SBC-CF, SBC-TL, and SBC-DCM active layers were carefully explored by the tilt resonant soft X-ray scattering (R-SoXS), thickness dependent light absorption, and secondary ion mass spectrometry (SIMs). The results indicate that SBC-CF and SBC-TL films have more mixed-phase region and lower phase purity. On the contrary, for the SBC-DCM film, angle-dependent grazing incident wide-angle X-ray scattering (GIWAXS) measurement reveals that there is a pure D18 layer near the substrate since it is only seen at larger incident angle, which is a solid evidence to confirm that it is true planar heterojunction structure. The SBC-DCM OSCs offered a similar PCE compared with the SBC-CF ones despite significant morphological changes between them, which is the best performance in truly planar heterojunction devices. Results show that the SBC-DCM devices achieved the longest exciton diffusion distance, higher V_{oc}, and similar recombination characteristics compared to the SBC-CF OSCs, which corresponds to their similar PCEs and high morphological tolerance. Our work indicates that the vertical phase separation can be effectively optimized by well-controlling film formation rate and time via the selection of solvents with different boiling points, and thus achieving favorable morphology and superior PCEs in OSCs.

2. Results and Discussion

2.1. Photovoltaic Performances

The schematic diagram of blade-coating technique is illustrated in **Figure 1**a. The chemical structures of D18 and YSe are shown in Figure 1b, and the corresponding UV–vis absorption spectra of neat films and active layers are displayed in Figure S1 (Supporting Information) and Figure 1c, respectively. The D18 film exhibits strong absorption in 400–700 nm and YSe film possesses strong absorption in 700–950 nm, showing an excellent complementary absorption. The characteristic peaks of YSe display a slight blue-shift in SBC-TL and SBC-DCM films in comparison with SBC-CF film, implying the decreased aggregation. Then, the OSCs were fabricated based on different solvents processed D18/YSe active layers, and the related current density and voltage (J–V) curves and detailed photovoltaic parameters were summarized in Figure 1d, **Table 1**, and Table S1 (Supporting Information), respectively. Meanwhile, the photovoltaic parameters of large-area devices are shown in the Table S2 and Figure S2

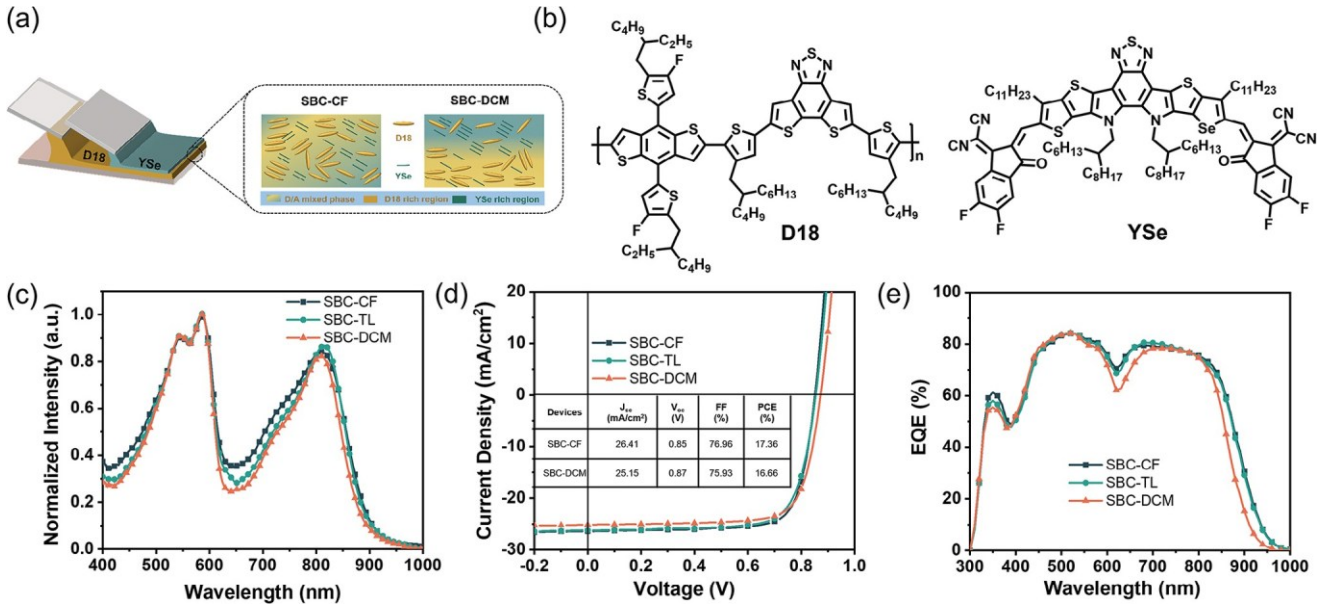

Figure 1. a) Diagrams of SBC technology for preparing SBC-CF and SBC-DCM active layers and the corresponding morphologies. b) Chemical structures of D18 and YSe. c) Normalized UV–vis absorption spectra of SBC active layers. d) *J–V* characteristics and e) related EQE curves of SBC devices.

(Supporting Information). Among these OSCs, the SBC-CF based ones obtained a superior PCE of 17.36% with a higher short-circuit current density (J_{sc}) and fill factor (FF) values, which is comparable to the standard BHJ devices (Table S1, Supporting Information). Besides, the SBC-TL based devices achieved a decent PCE of 16.76%. While the SBC-DCM based ones obtained an equivalent PCE of 16.66% with a much higher open-circuit voltage (V_{oc}), suggesting that it most resembles a planar structure. Meanwhile, the lower J_{sc} in the SBC-DCM based devices also partially confirms their planar structure of active layers, mainly due to the fewer D/A interfaces. The integrated J_{sc} values agree well with those obtained from *J–V* characterizations (Figure 1e). Furthermore, the hole mobility (μ_h) and electron mobility (μ_e) values of OSCs were measured by using space-charge-limited current (SCLC) method on the basis of the Mott–Gurney equation. The specific curves and corresponding values are shown in Figure S3 (Supporting Information) and Table 1. Results show that the SBC-CF and SBC-TL based devices shown the similar μ_e and μ_h values, and the SBC-DCM based devices have lower values.

2.2. Physical dynamics

Meanwhile, the photoluminescence (PL) spectra were used to probe the features of quenching behaviors of photoactive films. As shown in **Figure 2**a, the SBC-CF films exhibit a weaker PL intensity with respect to the other films, indicating a low recombination during their rapid charge transfer for achieving a higher J_{sc} in OSCs. To understand the charge generation and recombination characteristics of OSCs, their light intensity-dependent V_{oc} and J_{sc} measurements were carried out to further clarify the improved photovoltaic performance (Figure 2b,c; Table S3, Supporting Information). The V_{oc} versus the natural logarithm of light intensity gives the slope (S) close to k_BT/q, where k_B, T, and q are the Boltzmann constant, temperature in Kelvin, and the elementary charge, respectively. The S is close to 1 k_BT/q if bimolecular recombination is dominant, while it is close to 2 k_BT/q if the trap-assisted recombination plays a leading role.[38] The fitted slopes are 1.16, 1.24, and 1.15 k_BT/q for the devices based on SBC-CF, SBC-TL, and SBC-DCM, respectively. Meanwhile, the relationship between J_{sc} and P_{light} can be described by the equation

Table 1. Photovoltaic performance parameters of the SBC devices under AM 1.5G 100 mW cm^{-2} illumination.

Devices	V_{oc} [V]	J_{sc} [mA/cm^2]	FF [%]	PCE[a)] [%]	μ_h [cm^{-2} V^{-1} s^{-1}]	μ_e [cm^{-2} V^{-1} s^{-1}]	μ_h/μ_e
SBC-CF	0.852	26.41	76.96	17.36 (17.15 ± 0.24)	3.52×10^{-4}	3.24×10^{-4}	1.08
SBC-TL	0.854	26.22	74.74	16.76 (16.49 ± 0.29)	3.11×10^{-4}	3.03×10^{-4}	1.03
SBC-DCM	0.873	25.15	75.93	16.66 (16.23 ± 0.25)	2.06×10^{-4}	1.78×10^{-4}	1.16

[a)] The average PCEs with standard deviation were calculated from 15 devices in each case.

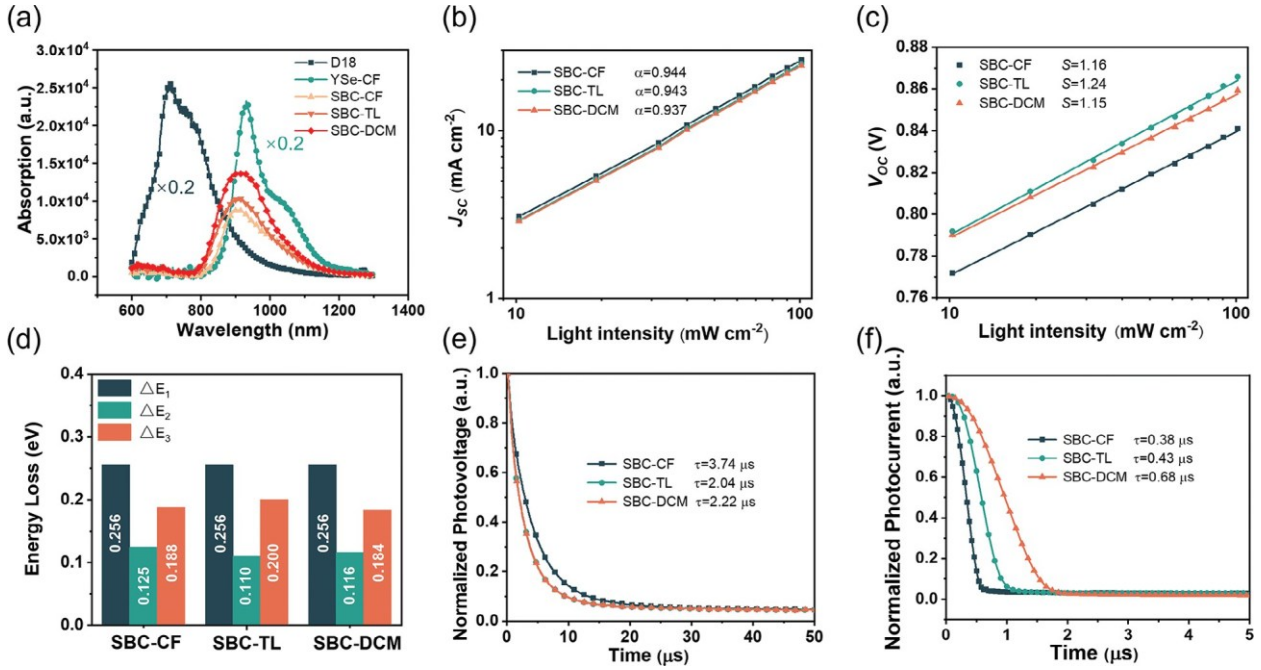

Figure 2. a) The PL spectra of pure films and related SBC active layers. The dependence of b) Jsc and c) Voc on light intensity of the SBC devices, respectively. d) Detailed Eloss values of SBC devices. e) TPV and f) TPC characteristic curves of the SBC devices, respectively.

$J_{sc} \propto (P_{light})^{a}$, where the power–law exponent a close to 1 represents a negligible bimolecular recombination.[39] The fitted a values are 0.944, 0.943, and 0.937 for the OSCs based on SBC-CF, SBC-TL, and SBC-DCM, respectively. The light intensity-dependent measurements suggesting that the trap-assisted and bimolecular recombination characteristics of the DCM-processed devices perform similarly to the CF-processed OSCs, which is part of the reason for their close performance.

The energy losses (E_{loss}) of the SBC devices were investigated to probe the effect of processed solvents on V_{oc} values, and the detailed E_{loss} values are summarized in Table S4 (Supporting Information). The energy bandgaps (E_g) of devices have been calculated via their emission and absorption spectra (Figure S4, Supporting Information). The E_{loss} analysis was determined according to Fourier transform photocurrent spectroscopy external quantum efficiency (FTPS-EQE) and electroluminescence quantum efficiency (EL) spectrum (Figure S5, Supporting Information). The total E_{loss} can be attributed to three parts as following equation:

$$\begin{aligned} E_{loss} &= E_g - qV_{OC} \\ &= \left(E_g - qV_{OC}^{SQ}\right) + \left(qV_{OC}^{SQ} - qV_{OC}^{rad}\right) + \left(qV_{OC}^{rad} - qV_{OC}\right) \\ &= \left(E_g - qV_{OC}^{SQ}\right) + q\Delta V_{OC}^{rad} + q\Delta V_{OC}^{non-rad} \\ &= \Delta E_1 + \Delta E_2 + \Delta E_3 \end{aligned} \quad (1)$$

where E_g is the bandgap, q is the elementary charge, V_{OC}^{SQ} is the maximum voltage based on the Shockley–Queisser limit (SQ limit), V_{OC}^{rad} is the open-circuit voltage when there is only radiative recombination, ΔV_{OC}^{rad} is the voltage loss of radiative recombination from the absorption below the E_g, and $\Delta V_{OC}^{non-rad}$ is the voltage loss of non-radiative recombination.[40] Among these devices, the SBC-CF based one offered a higher radiative recombination loss, which is partly explains their lower V_{oc}. Meanwhile, the SBC-DCM based device exhibited a lower E_{loss} compared with the SBC-CF based one, leading to a higher V_{oc}. The higher V_{oc} is one of the reasons for the similar PCE of the SBC-CF and SBC-DCM devices. Each part of E_{loss} of the OSCs based on SBC-CF, SBC-TL, and SBC-DCM were summarized in Figure 2d. Furthermore, the charge recombination dynamics and charge extraction process of the devices were studied via transient photo-voltage (TPV) and transient photo-current (TPC) measurements, respectively, and the corresponding carrier lifetime of devices can be estimated from the exponential voltage decay. The equation for carrier lifetime in TPV analysis is a mono-exponential:

$$V = A \exp\left(-\frac{t}{\tau}\right) \quad (2)$$

where A is a constant that fits to the peak height, t is time, and τ is decay time constant, respectively.[41,42] As shown in Figure 2e, the SBC-CF based devices gained a longer carrier lifetime of 3.74 μs compared to the devices based on SBC-TL (2.04 μs) and SBC-DCM (2.22 μs), indicating a reduced bimolecular recombination process.[43] In addition, the TPC technique was conducted to study the charge extraction properties of the SBC devices (Figure 2f). The charge extraction times of the devices based on SBC-CF, SBC-TL, and SBC-DCM were extracted to be 0.38, 0.43, and 0.68 μs, respectively. The shorter charge extraction lifetime in the SBC-CF devices suggests that the photo-generated

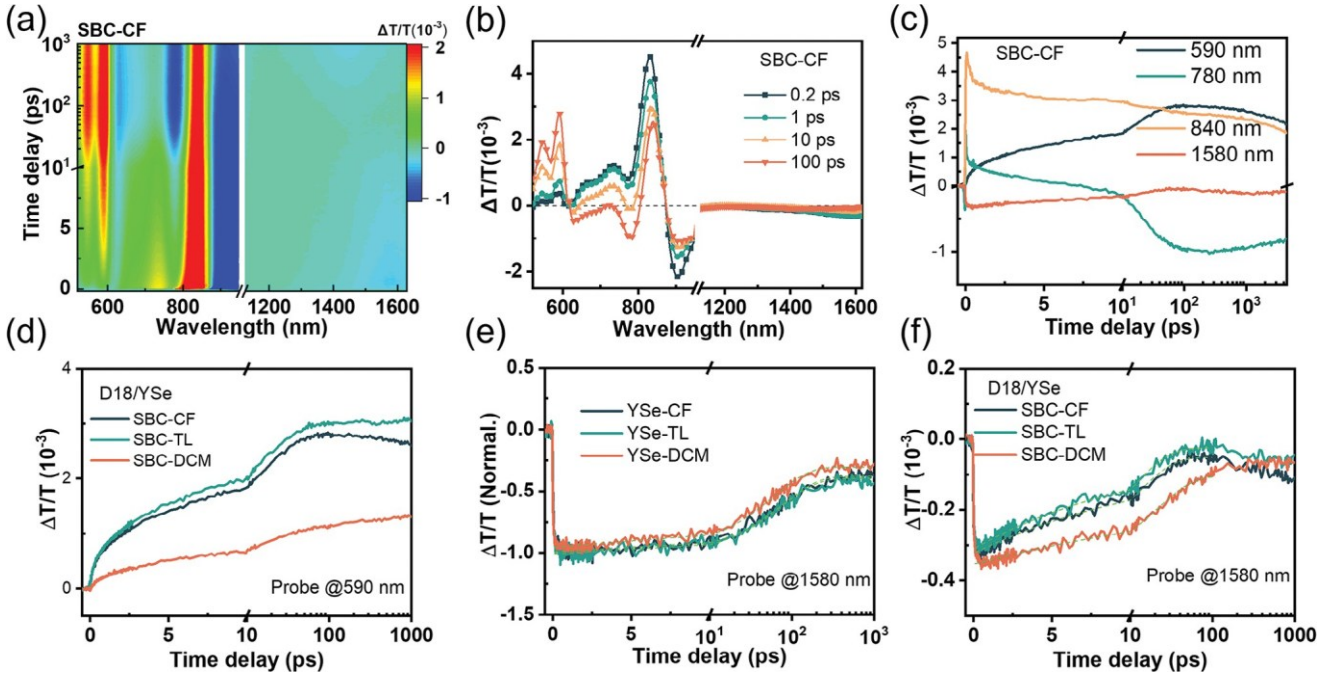

Figure 3. a) TA data recorded from SBC-CF active layer under a 800 nm excitation. b) TA spectra of the SBC-CF active layer at different delay times. c) TA dynamics at different wavelengths in the SBC-CF active layer. d) Under a 590 nm excitation, TA dynamics of the GSB signal of donor in the D18/YSe active layers processed with different solvents. TA dynamics of i-EX states at 1580 nm in e) the neat YSe neat films and f) the D18/YSe active layers processed with different solvents.

carriers are extracted more efficiently.[44,45] To gain insight into why the SBC-CF and SBC-DCM based devices have similar device performance, the exciton diffusion distance was obtained by carrying out a device structure of ITO/CuSCN/acceptor/Phen-NaDPO/Al and measuring the related EQE calculation with different film thicknesses.[46] Based on the EQE plots (Figure S6, Supporting Information), the exciton diffusion distance were calculated to be 25, 20, and 30 nm for the devices based on YSe processed with CF, TL, and DCM, respectively. The above result indicates that the SBC-DCM based devices have the longest exciton diffusion distance from YSe component, offering a higher morphological tolerance.

To get more information of the photo-induced charge transfer and recombination in OSCs, the transient absorption (TA) spectroscopy measurements were employed to study the charge generation dynamics in both the neat YSe and related SBC active layers processed with different solvents. **Figure 3** and Figures S7–S12 (Supporting Information) show the TA data of the D18/YSe active layers of selective acceptor excitation, where the charge generation is triggered by hole transfer from YSe to D18. In accordance with the absorption spectrum of YSe, upon excitation, the ground bleaching signal (GSB) of ≈840 nm appears (Figure 3a; Figures S7 and S8, Supporting Information). In addition, two excited states absorption bands of ≈920 and ≈1580 nm are observed in both the neat YSe films and related SBC active layers (Figure 3b; Figures S7 and S8, Supporting Information), representing the local excitation (LE) states and intra-moiety excited (i-EX) states respectively. As depicted in Figure 3e, the neat YSe films processed with CF (≈77.6 ps) and TL (≈75.1 ps) exhibit longer lifetimes of i-EX states compared to the one processed with DCM (≈60.2 ps), implying the improved hole transfer and superior crystallization in the SBC-CF and SBC-TL active layers. The rises of the GSB signal from D18 at 590 nm, ESA signal of charge separation states at 780 nm, and the corresponding decay of the GSB and the ESA signals of i-EX states of YSe suggest the ongoing hole transfer process (Figure 3c). The SBC-CF and SBC-TL active layers have much faster hole transfer with the lifetimes of ≈14.7 and ≈13.3 ps compared to the SBC-DCM one with a lifetime of ≈33.7 ps (Figure 3d,f; **Table 2**). These results suggest that the improved hole transfer property is partially the reason for the higher PCE of SBC-CF based devices.[18,47,48]

2.3. Molecule Packing and Vertical Phase Separation

In order to better understand morphology characteristics, GIWAXS measurement was adopted to provide the information of molecular ordering.[49,50] 2D GIWAXS patterns and the corresponding line-cuts profiles are depicted in **Figure 4**a–c and

Table 2. The hole transfer kinetics in SBC active layers.

Samples	τ_A (ps)[a]	τ_{SBC} (ps)[a]	$\tau_{hole\ transfer}$ (ps)[b]
SBC-CF	77.6	12.4	14.7
SBC-TL	75.1	11.3	13.3
SBC-DCM	60.2	21.6	33.7

[a] mono-exponential fitting; [b] $\frac{1}{\tau_{hole\ transfer}} = \frac{1}{\tau_{SBC}} - \frac{1}{\tau_A}$.

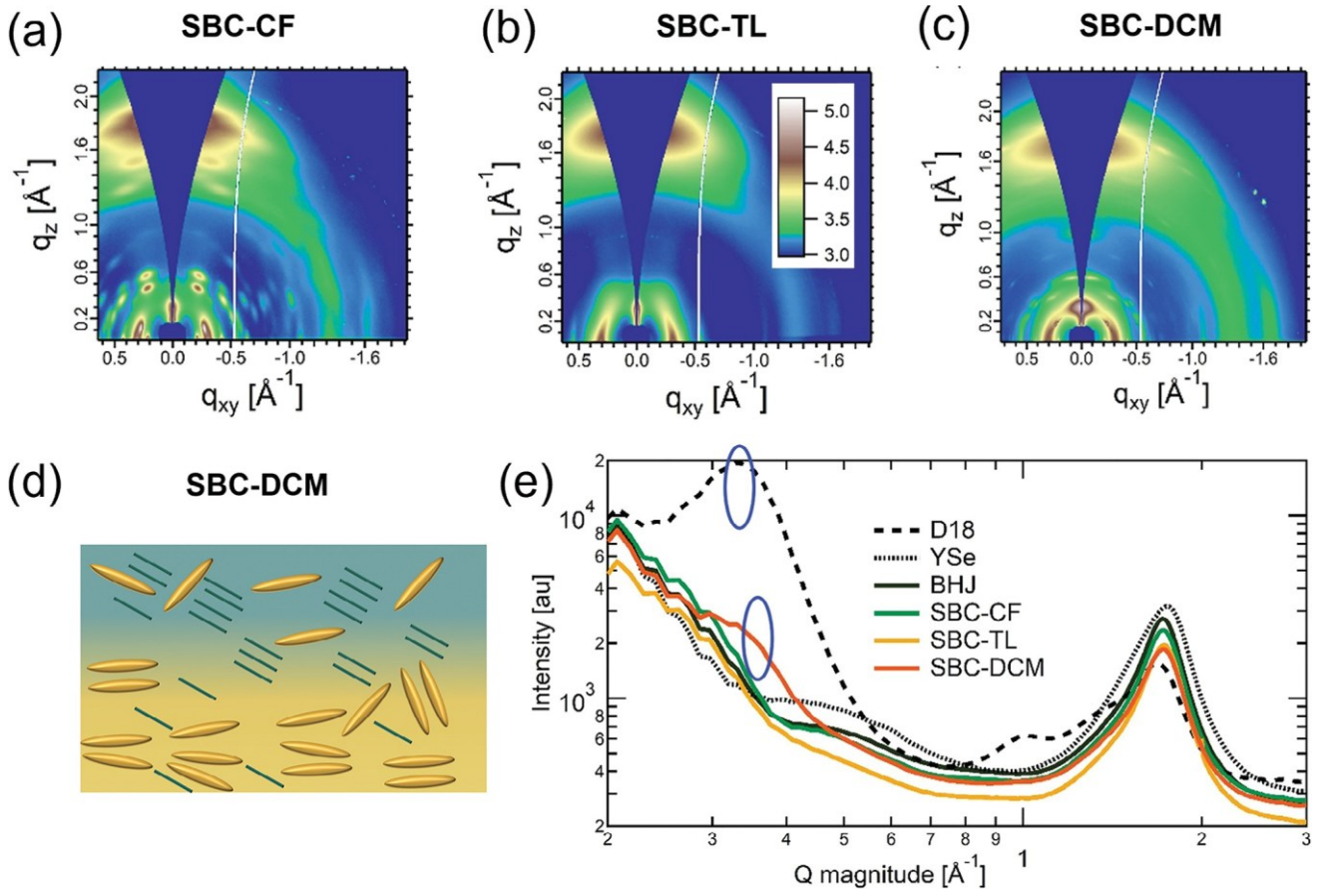

Figure 4. a–c) 2D GIWAXS patterns of SBC active layers with YSe top layer cast from CF, TL, and DCM, respectively. d) Schematic diagram of the morphology of SBC-DCM active layer. e) The OOP line-cuts from 2D GIWAXS profiles of D18 and YSe pure films, as well as related BHJ and SBC active layers at an incident angle of $\alpha = 0.31°$. The portion circled in blue highlights diffraction from pure D18 crystals that only emerge in the DCM film. More details and data in the Supporting Information.

Figure S13, Supporting Information. The YSe pure film exhibits a highly ordered lamellar stacking (100) peak at low q (0.30 and 0.42 Å^{-1}) in the in-plane (IP) direction, while its strong and sharp (010) diffraction peak at 1.76 Å^{-1} in the out-of-plane (OOP) direction indicates a preferential "face-on" orientation. To verify the SBC-DCM active layer is truly planar heterojunction, the GIWAXS measurements were performed by using the incident angles of 0.05° to 0.31° in increasing increments of 0.02° (Figures S14 and S15, Supporting Information). The critical angle for carbon at 10 keV is 0.13°, below critical incident angle measures just top ≈10 nm, and above critical angle expect to measure both layers. By comparing all samples, the following conclusions can be drawn: 1) At shallow incidence, they are nearly identical and are already showing signs of D18, which suggests that there is mixing in the top layer; 2) When the YSe dissolved in CF and in TL is cast on top of D18, the traces appear identically to the BHJ; 3) The difference in the SBC-DCM active layer is a D18 feature at 0.31 Å^{-1} after the critical angle (Figure 4e). The above results suggest that there is a pure D18 layer near the substrate, as it is only visible at higher incident angle, which is solid evidence to substantiate that the SBC-DCM active layer is a truly planar heterojunction (Figure 4d).

In order to provide further evidence of vertical structure within the active layer, -R-SoXS-[51] was carried out in a tilted geometry to investigate the vertical component distribution and phase separation properties.[52] To address the problem that the data collected by R-SoXS in conventional normal-incidence transmission mode lacks vertical morphology information of active layers, the sample holder is 70° away from normal incidence, increasing the component of the scattering vector in the direction perpendicular to the active layer (**Figure 5**a). The characterization results can further guide the regulation of the vertical structure and make the photoelectric conversion process more efficient. Figure 5 shows the intensity profiles of traditional R-SoXS comparing resonant scattering using 284.4 eV X-rays versus non-resonant 270 eV. All samples, including a traditional BHJ, show a scattering feature in the range of $q = 0.1–0.4$ nm^{-1} which roughly corresponds to domains with an in-plane periodicity (characteristic length) from 20–60 nm calculated by $L_C = 2\pi/q$. The enhanced signals over non-resonant profiles indicate that these signals originate from phase-separated domains of donor–rich and acceptor–rich, which also indicates mixing occurs in SBC devices. A much stronger feature centered at a higher $q = 0.3$ nm^{-1} ($L_C = 20$ nm) than the others indicate that the SBC-DCM active layer has the smallest in-plane phase separation and the

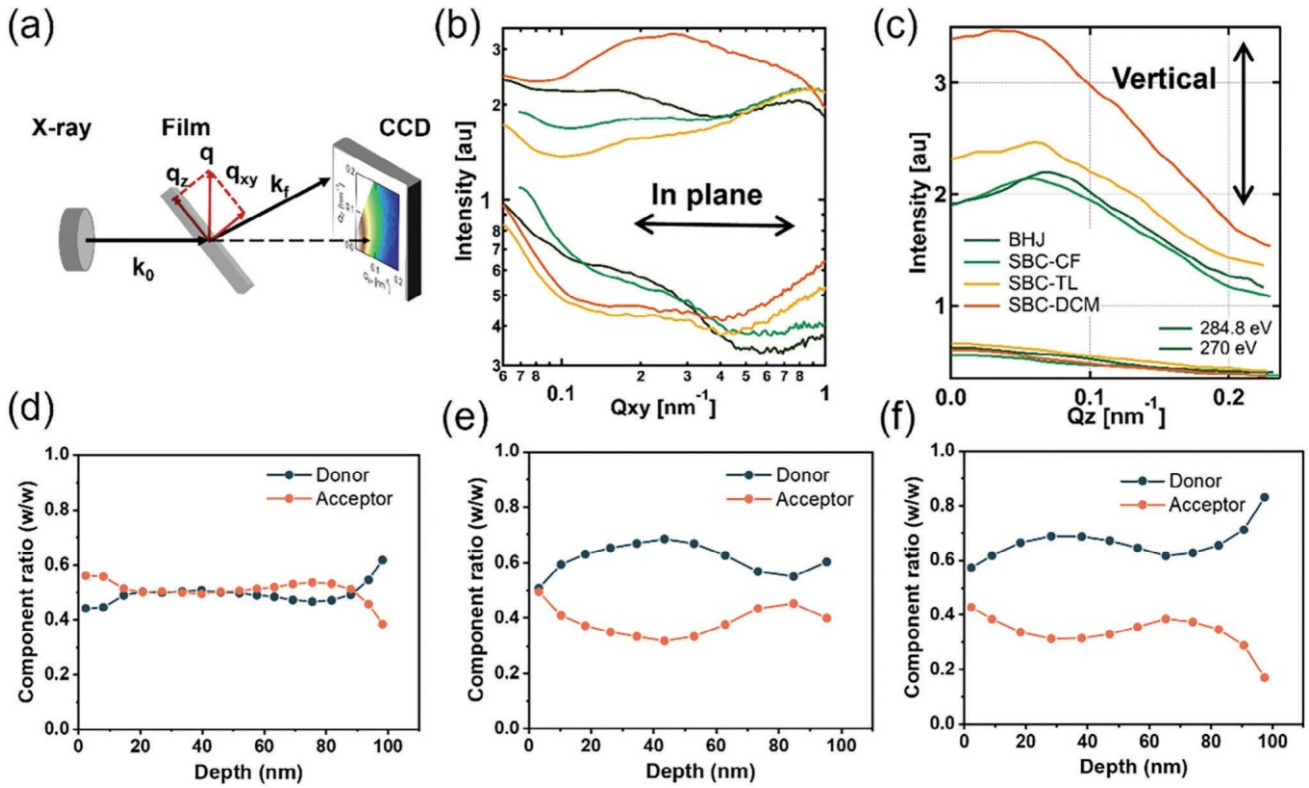

Figure 5. a) The diagram of tilt R-SoXS scattering system. a) Traditional R-SoXS profiles which are sensitive to in-plane domain structure, as shown in the inset schematic. c) Q_z scattering profiles from tilted R-SoXS measurements with an inset of schematic depicting the vertical heterogeneity, acquired in the range of Q_{xy} = 0.1-0.3 nm^{-1}. Full *q*–maps were depicted in the Supporting Information. d–f) Relative concentration depth profiles from film-depth-dependent light absorption spectra for the SBC active layers with the YSe top layer cast from CF, TL, and DCB solvents, respectively.

highest phase purity (Figure 5b). The *q*–maps measured via tilt-RSoXS (Figure S16, Supporting Information) show an increased scattering intensity in the OOP (Q_z) direction for the SBC active layers compared with the control BHJ ones. The Q_z profiles extracted from these *q*–maps at the IP (Q_{xy}) location of the domain scattering features (L_C) are shown in Figure 5c, for probing the vertical structure within the active layers. Here, a feature at Q_z of ≈0.06 nm^{-1} may indicate scattering from the film thickness of 100 nm. Significant enhancement of scattering in the SBC-DCM active layer out to a higher *q* is consistent with the increased vertical structure revealed in the GIWAXS data.

The surface morphology of active layers was also studied by performing the atomic force microscope (AFM) characterization. As shown in Figure S17 (Supporting Information), the uniform fiber distribution can be found in the SBC-CF, SBC-TL, and SBC-DCM active layers, and the corresponding specific values of root-mean-square (RMS) roughness were measured as 2.47, 1.59, and 1.45 nm, respectively. The fibril textures in all the SBC active layers resemble D18 surface fibrils rather than YSe surface structures, which provides further evidence of mixing at the top of the active layers.

The thickness-dependent light absorption[53] was recorded to study the effects of sequential deposition for three SBC active layers processed with different solvents with depth-dependent composition (Figure 5d–f). According to their absorption spectra (Figure S18a–c, Supporting Information), the peak centered at 590 nm is originated from D18 and the peak located at 830 nm is originated from YSe. The composition and corresponding film depth for each spectrum were depicted in Figure S18d–f (Supporting Information). Based on this analysis, the SBC-CF active layer is the most mixed throughout the depth of active layer. However, it has an enhanced acceptor (YSe) concentration at the top surface and an enhanced donor (D18) concentration at the bottom surface, which tends to enhance charge extraction at the electrodes. On the contrary, there is an increased evolution of the donor/acceptor concentration with depth in the SBC-TL and SBC-DCM active layers, with the purest donor (D18) located at the bottom surface, which agrees with the GIWAXS analysis. -SIMS-[54] is used as a final measurement to detect the differences in the vertical distribution of active layers. Here, the selenium (Se) atomic and cyano (CN) group belong to YSe component can be chosen as the characteristic elements to analyze their vertical distribution. As shown in Figures S19–S21 (Supporting Information), the intensity of Se signal is evenly distributed in the SBC-CF and SBC-TL active layers. Otherwise, it prefers to enrich in the upper part of the SBC-DCM active layers. Benefited to their above morphologies, the crack-onset strain (COS) of the SBC-CF, SBC-TL, and SBC-DCM active layers are measured as 8.5%, 7.9%, and 13.5%, respectively, as shown in Figure S22 (Supporting Information). Such excellent properties are desired for realizing high-efficiency flexible devices.

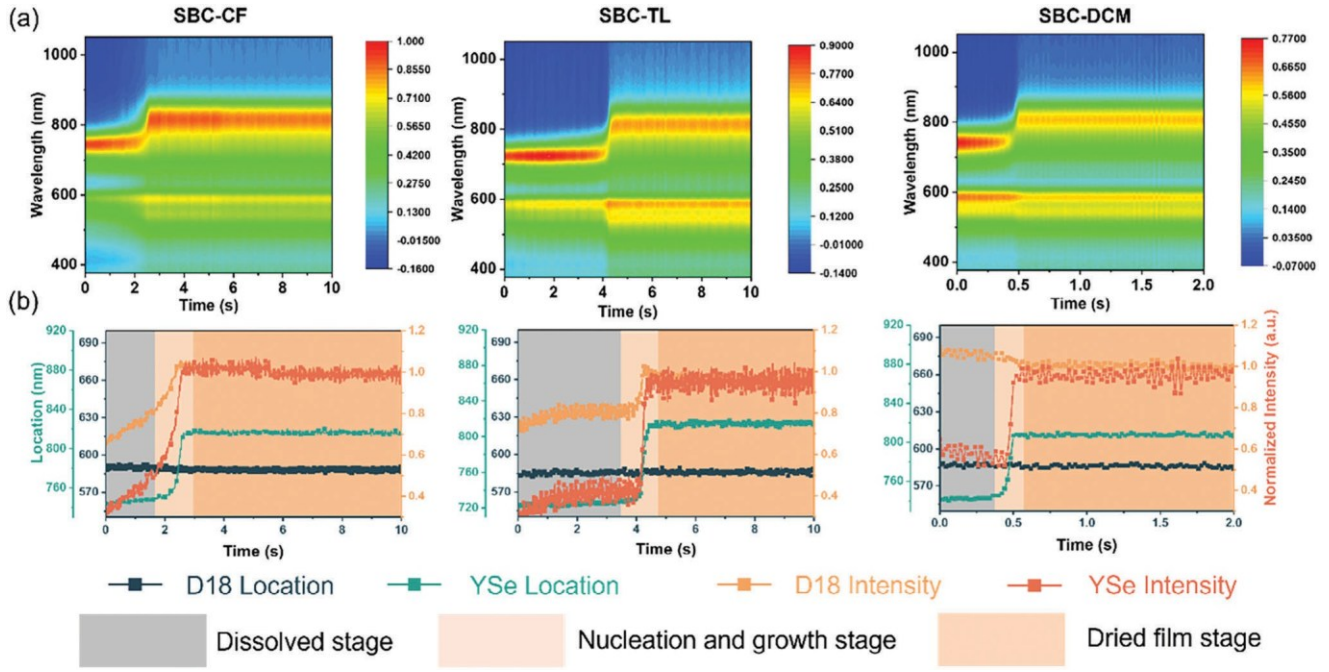

Figure 6. a) Color contour maps of UV–vis absorption spectra during the deposition process. b) Plotting of the 0-0 absorption peak intensity of D18 and YSe, as well as the position of D18 and YSe as a function of film forming time during blade-coating.

2.4. In-Situ Morphology Studies

For the OSCs processed by solution method, the structural evolution process active layer from solution to film is very important. Here, in situ UV–vis absorption[55] measurements were employed to clarify the aggregation evolution caused by processing solvents. **Figure 6a** depicts the 2D absorption patterns of active layers, while the corresponding peak intensity and location evolution are demonstrated in Figure 6b. The film-forming process can be divided into three stages, including dissolved stage, nucleation and growth stage, and dried film stage, respectively. The first stage is pre-aggregation process where solvent evaporates and the concentration of the solution increases. In the second stage, the intensity of donor absorption increases during the film-forming process in the SBC-CF and SBC-TL active layers. Differently, the intensity of donor absorption remains constant during the whole process in the SBC-DCM active layer, indicating that there is no effect on D18 during sequential deposition. At the third stage, the peak intensity and location parameters of active layer materials are fixed. The slope of the peak location changed with time reflects the aggregation rate. According to the calculation, the aggregation rates of YSe and D18 were determined to be 0.253 and 0.12 for the SBC-CF active layer, and 0.15 and 0.05 for the SBC-TL active layer. (The fitting region is the nucleation and growth stage) We speculate that the balanced crystallization kinetics of the SBC-CF based devices are favorable toward realizing a higher PCE through improving charge transport processes. During the film-forming process of active layers, phase separation is an important factor that affects device performance. The in situ PL[34] can reflect this process in real-time, and the related dominant factors of phase separation process can be understood by characterizing the changes of phase region size and aggregation degree during solvent volatilization. **Figure 7a** shows the time evolution of PL contour maps for these SBC active layers processed with different solvents. The extracted peak location and integrated PL intensity were depicted in Figure 7b. Here, the excitation wavelength is 532 nm, which can exclusively excite D18. In this work, the phase separation evolution of the SBC active layers can be divided into two stages, namely the quenching stage and the dried film stage. At the first stage, the average distance between the homogeneously distributed fluorophores and quencher molecules decreases with increasing the relative volume concentration of the nonvolatile materials, resulting in a sharply reduced the integral PL intensity. At this stage, the quenching rate can reflect the phase separation rate. Since the donor and acceptor components are almost completely blended in CF, both the PL intensities of D18 and YSe go nearly to zero at the end of this stage for the SBC-CF active layer compared with those PL intensities in the other samples, resulting the same quenching efficiency. Due to the lower degree of co-mixture between donor and acceptor components in the SBC-TL and SBC-DCM active layers, the different separation speeds can be found. Furthermore, the phase separation can be reflected by quenching intensity. The quenching intensity decreases gradually in the SBC-CF, SBC-TL, and SBC-DCM active layers, suggesting their increased phase separation.

3. Conclusion

In conclusion, we develop a way to modulate the vertical structure of active layer for boosting the charge transfer property and thus PCE of OSCs. By changing the processing solvent of the acceptor and controlling the infiltration degree of the upper layer, the grading distribution of the donor and the acceptor was realized.

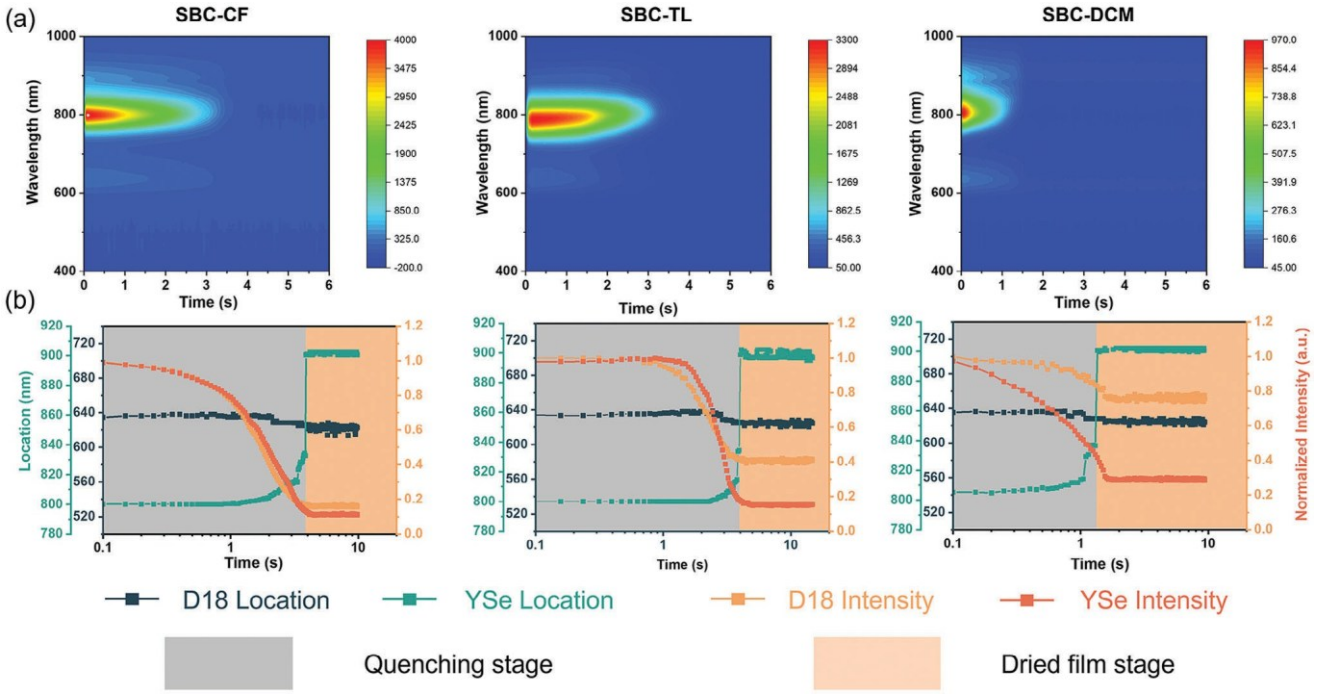

Figure 7. a) Time-dependent contour maps of PL spectra during the deposition process of active layers. b) Time evolution of film integral PL intensity and peak location of SBC active layers.

Results show that when using CF as a solvent to prepare acceptor upper layer, the crystallinity of acceptor increases with changes in phase size and purity, which are beneficial for improving charge transport and decreasing the bimolecular recombination. Courtesy to the favorable molecular crystallinity and phase separation, the best performing OSCs with a PCE of 17.36% was obtained. Meanwhile, a suite of characterization techniques were carried out to probe the vertical structure of the SBC active layers. Angle-dependent GIWAXS measurement reveals that the SBC-DCM active layer is true planar heterojunction structure. Despite significant morphological varies, the SBC-DCM based devices achieved a similar PCE compared with the SBC-CF based devices, demonstrating a high morphological tolerance. This work proposal a strategy to optimize the vertical structure of active layer for further boosting the photovoltaic performance of OSCs processed via rapid film-forming and SBC method.

Supporting Information

Supporting Information is available from the Wiley Online Library or from the author.

Acknowledgements

Thanks for the support from the National Key Research and Development Program of China (2022YFE0132400), the National Key R&D Plan Project (Grant No. 2022YFB4200305), NSFC (21875182, 52173023, 22309143, W2411049), the Key Scientific and Technological Innovation Team Project of Shaanxi Province (2020TD-002), the China National Postdoctoral Program for Innovative Talent (BX2021232), the China Postdoctoral Science Foundation (2023M742761), and 111 project 2.0 (BP0618008). BAC, TM, and AP acknowledge the funding support by the US National Science Foundation Grant #2247711. X-ray data was acquired at beamlines 7.3.3 and 11.0.1.2 at the Advanced Light Source, which is supported by the Director, Office of Science, Office of Basic Energy Sciences, of the U.S. Department of Energy under Contract No. DE-AC02-05CH11231. The authors thank Dr. Eric Schaible and Dr. Chenhui Zhu at beamline 7.3.3.

Conflict of Interest

The authors declare no conflict of interest.

Data Availability Statement

The data that support the findings of this study are available from the corresponding author upon reasonable request.

Keywords

organic solar cells, sequential blade-coating, solvent, vertical structure

Received: August 23, 2024
Revised: October 13, 2024
Published online: November 7, 2024

[1] T. Lin, Y. Hai, Y. Luo, L. Feng, T. Jia, J. Wu, R. Ma, T. A. Dela Peña, Y. Li, Z. Xing, M. Li, M. Wang, B. Xiao, K. S. Wong, S. Liu, G. Li, *Adv. Mater.* **2024**, *36*, 2312311.
[2] C. Guo, Y. Sun, L. Wang, C. Liu, C. Chen, J. Cheng, W. Xia, Z. Gan, J. Zhou, Z. Chen, J. Zhou, D. Liu, J. Guo, W. Li, T. Wang, *Energy Environ. Sci.* **2024**, *17*, 2492.

[3] R. Basu, F. Gumpert, J. Lohbreier, P.-O. Morin, V. Vohra, Y. Liu, Y. Zhou, C. J. Brabec, H.-J. Egelhaaf, A. Distler, *Joule* **2024**, *8*, 970.
[4] H. Zhang, Y. Liu, G. Ran, H. Li, W. Zhang, P. Cheng, Z. Bo, *Adv. Mater.* **2024**, *36*, 2400521.
[5] F. Yi, M. Xiao, Y. Meng, H. Bai, W. Su, W. Gao, Z. F. Yao, G. Qi, Z. Liang, C. Jin, L. Tang, R. Zhang, L. Yan, Y. Liu, W. Zhu, W. Ma, Q. Fan, *Angew. Chem., Int. Ed.* **2024**, *63*, 2023192.
[6] T. Duan, W. Feng, Y. Li, Z. Li, Z. Zhang, H. Liang, H. Chen, C. Zhong, S. Jeong, C. Yang, S. Chen, S. Lu, O. A. Rakitin, C. Li, X. Wan, B. Kan, Y. Chen, *Angew. Chem., Int. Ed.* **2023**, *62*, 2023088.
[7] X. He, Z. X. Liu, H. Chen, C. Z. Li, *Adv. Mater.* **2023**, *36*, 2306681.
[8] Z. Chen, J. Zhu, D. Yang, W. Song, J. Shi, J. Ge, Y. Guo, X. Tong, F. Chen, Z. Ge, *Energy Environ. Sci.* **2023**, *16*, 3119.
[9] H. Lu, W. Liu, G. Ran, Z. Liang, H. Li, N. Wei, H. Wu, Z. Ma, Y. Liu, W. Zhang, X. Xu, Z. Bo, *Angew. Chem., Int. Ed.* **2023**, *135*, 202314420.
[10] Q. Wu, Y. Yu, X. Xia, Y. Gao, T. Wang, R. Sun, J. Guo, S. Wang, G. Xie, X. Lu, E. Zhou, J. Min, *Joule* **2022**, *6*, 2138.
[11] H. Zhang, G. Ran, X. Cui, Y. Liu, Z. Yin, D. Li, X. Ma, W. Liu, H. Lu, R. Liu, L. Cai, W. Zhang, S. Guo, H. Li, J. Yu, Y. Lin, Y. Liu, G. Lu, Z. Ma, P. Cheng, Z. Bo, *Adv. Energy Mater.* **2023**, *13*, 2302063.
[12] Q. Fan, R. Ma, J. Yang, J. Gao, H. Bai, W. Su, Z. Liang, Y. Wu, L. Tang, Y. Li, Q. Wu, K. Wang, L. Yan, R. Zhang, F. Gao, G. Li, W. Ma, *Angew. Chem., Int. Ed.* **2023**, *62*, 202308307.
[13] H. Bai, R. Ma, W. Su, T. A. D. Peña, T. Li, L. Tang, J. Yang, B. Hu, Y. Wang, Z. Bi, Y. Su, Q. Wei, Q. Wu, Y. Duan, Y. Li, J. Wu, Z. Ding, X. Liao, Y. Huang, C. Gao, G. Lu, M. Li, W. Zhu, G. Li, Q. Fan, W. Ma, *Nano-Micro Lett.* **2023**, *15*, 241.
[14] H. Xia, Y. Zhang, K. Liu, W. Deng, M. Zhu, H. Tan, P. W. K. Fong, H. Liu, X. Xia, M. Zhang, T. A. P. Dela Peña, R. Ma, M. Li, J. Wu, Y. Lang, J. Fu, W.-Y. R. Wong, X. Lu, W. Zhu, G. Li, *Energy Environ. Sci.* **2023**, *16*, 6078.
[15] C. Guo, Y. Fu, D. Li, L. Wang, B. Zhou, C. Chen, J. Zhou, Y. Sun, Z. Gan, D. Liu, W. Li, T. Wang, *Adv. Mater.* **2023**, *35*, 2304921.
[16] S. Li, C. He, T. Chen, J. Zheng, R. Sun, J. Fang, Y. Chen, Y. Pan, K. Yan, C.-Z. Li, M. Shi, L. Zuo, C.-Q. Ma, J. Min, Y. Liu, H. Chen, *Energy Environ. Sci.* **2023**, *16*, 2262.
[17] H. Lai, H. Chen, Z.-Y. Chen, Y. Lang, Y. Zhu, S.-T. Zhang, X. Lai, P. Tan, Y. Zhang, B. Yang, G. Li, F. He, *Energy Environ. Sci.* **2023**, *16*, 5944.
[18] C. He, Y. Pan, Y. Ouyang, Q. Shen, Y. Gao, K. Yan, J. Fang, Y. Chen, C.-Q. Ma, J. Min, C. Zhang, L. Zuo, H. Chen, *Energy Environ. Sci.* **2022**, *15*, 2537.
[19] Z. Zhong, S. Chen, J. Zhao, J. Xie, K. Zhang, T. Jia, C. Zhu, J. Jing, Y. Liang, L. Hong, S. Zhu, D. Ma, F. Huang, *Adv. Energy Mater.* **2023**, *13*, 2302273.
[20] J. Wang, Y. Wang, K. Xian, J. Qiao, Z. Chen, P. Bi, T. Zhang, Z. Zheng, X. Hao, L. Ye, S. Zhang, J. Hou, *Adv. Mater.* **2024**, *36*, 2305424.
[21] F. Cheng, Y. Cui, F. Ding, Z. Chen, Q. Xie, X. Xia, P. Zhu, X. Lu, H. Zhu, X. Liao, Y. Chen, *Adv. Mater.* **2023**, *35*, 2300820.
[22] S. Lai, Y. Cui, Z. Chen, X. Xia, P. Zhu, S. Shan, L. Hu, X. Lu, H. Zhu, X. Liao, Y. Chen, *Adv. Mater.* **2024**, *36*, 2313105.
[23] D. He, J. Zhou, Y. Zhu, Y. Li, K. Wang, J. Li, J. Zhang, B. Li, Y. Lin, Y. He, C. Wang, F. Zhao, *Adv. Mater.* **2024**, *36*, 2308909.
[24] R. Sun, J. Guo, Q. Wu, Z. Zhang, W. Yang, J. Guo, M. Shi, Y. Zhang, S. Kahmann, L. Ye, X. Jiao, M. A. Loi, Q. Shen, H. Ade, W. Tang, C. J. Brabec, J. Min, *Energy Environ. Sci.* **2019**, *12*, 3118.
[25] B. Zhang, F. Yang, S. Chen, H. Chen, G. Zeng, Y. Shen, Y. Li, Y. Li, *Adv. Funct. Mater.* **2022**, *32*, 2202011.
[26] Y. Zhang, K. Liu, J. Huang, X. Xia, J. Cao, G. Zhao, P. W. K. Fong, Y. Zhu, F. Yan, Y. Yang, X. Lu, G. Li, *Nat. Commun.* **2021**, *12*, 4815.
[27] H. Mao, L. Zhang, L. Wen, L. Huang, L. Tan, Y. Chen, *Adv. Funct. Mater.* **2022**, *33*, 2209152.
[28] Y. Wang, J. Xue, H. Zhong, C. R. Everett, X. Jiang, M. A. Reus, A. Chumakov, S. V. Roth, M. A. Adedeji, N. Jili, K. Zhou, G. Lu, Z. Tang, G. T. Mola, P. Müller-Buschbaum, W. Ma, *Adv. Energy Mater.* **2023**, *13*, 2203496.
[29] K. Weng, L. Ye, L. Zhu, J. Xu, J. Zhou, X. Feng, G. Lu, S. Tan, F. Liu, Y. Sun, *Nat. Commun.* **2020**, *11*, 2855.
[30] K. Jiang, J. Zhang, Z. Peng, F. Lin, S. Wu, Z. Li, Y. Chen, H. Yan, H. Ade, Z. Zhu, A. K. Jen, *Nat. Commun.* **2021**, *12*, 468.
[31] L. Zhan, S. Li, X. Xia, Y. Li, X. Lu, L. Zuo, M. Shi, H. Chen, *Adv. Mater.* **2021**, *33*, 2007231.
[32] X. Song, H. Xu, X. Jiang, S. Gao, X. Zhou, S. Xu, J. Li, J. Yu, W. Liu, W. Zhu, P. Müller-Buschbaum, *Energy Environ. Sci.* **2023**, *16*, 3441.
[33] L. Zhu, W. Zhong, C. Qiu, B. Lyu, Z. Zhou, M. Zhang, J. Song, J. Xu, J. Wang, J. Ali, W. Feng, Z. Shi, X. Gu, L. Ying, Y. Zhang, F. Liu, *Adv. Mater.* **2019**, *31*, 1902899.
[34] S. Engmann, F. A. Bokel, H. W. Ro, D. M. DeLongchamp, L. J. Richter, *Adv. Energy Mater.* **2016**, *6*, 1502011.
[35] X. Gu, H. Yan, T. Kurosawa, B. C. Schroeder, K. L. Gu, Y. Zhou, J. W. F. To, S. D. Oosterhout, V. Savikhin, F. Molina-Lopez, C. J. Tassone, S. C. B. Mannsfeld, C. Wang, M. F. Toney, Z. Bao, *Adv. Energy Mater.* **2016**, *6*, 1601225.
[36] Y. Wang, X. Wang, B. Lin, Z. Bi, X. Zhou, H. B. Naveed, K. Zhou, H. Yan, Z. Tang, W. Ma, *Adv. Energy Mater.* **2020**, *10*, 2000826.
[37] H. Zhao, H. B. Naveed, B. Lin, X. Zhou, J. Yuan, K. Zhou, H. Wu, R. Guo, M. A. Scheel, A. Chumakov, S. V. Roth, Z. Tang, P. Müller-Buschbaum, W. Ma, *Adv. Mater.* **2020**, *32*, 2002302.
[38] L. J. A. Koster, V. D. Mihailetchi, R. Ramaker, P. W. M. Blom, *Appl. Phys. Lett.* **2005**, *86*, 123509.
[39] T. Li, S. Dai, Z. Ke, L. Yang, J. Wang, C. Yan, W. Ma, X. Zhan, *Adv. Mater.* **2018**, *30*, 1705969.
[40] S. M. Menke, N. A. Ran, G. C. Bazan, R. H. Friend, *Joule* **2018**, *2*, 25.
[41] P. W. M. Blom, V. D. Mihailetchi, L. J. A. Koster, D. E. Markov, *Adv. Mater.* **2007**, *19*, 1551.
[42] Z. Li, F. Gao, N. C. Greenham, C. R. McNeill, *Adv. Funct. Mater.* **2011**, *21*, 1419.
[43] X. Du, T. Heumueller, W. Gruber, A. Classen, T. Unruh, N. Li, C. J. Brabec, *Joule* **2019**, *3*, 215.
[44] S. Wood, D. O'Connor, C. W. Jones, J. D. Claverley, J. C. Blakesley, C. Giusca, F. A. Castro, *Sol. Energy Mat. Sol. C.* **2017**, *161*, 89.
[45] J. Gao, A. F. Fidler, V. I. Klimov, *Nat. Commun.* **2015**, *6*, 8185.
[46] Y. Tang, H. Zheng, X. Zhou, Z. Tang, W. Ma, H. Yan, *Energy Environ. Sci.* **2023**, *16*, 653.
[47] Y. Cai, Y. Li, R. Wang, H. Wu, Z. Chen, J. Zhang, Z. Ma, X. Hao, Y. Zhao, C. Zhang, F. Huang, Y. Sun, *Adv. Mater.* **2021**, *33*, 2101733.
[48] R. Wang, J. Yuan, R. Wang, G. Han, T. Huang, W. Huang, J. Xue, H. C. Wang, C. Zhang, C. Zhu, P. Cheng, D. Meng, Y. Yi, K. H. Wei, Y. Zou, Y. Yang, *Adv. Mater.* **2019**, *31*, 1904215.
[49] P. Müller-Buschbaum, *Adv. Mater.* **2014**, *26*, 7692.
[50] B. A. Collins, J. E. Cochran, H. Yan, E. Gann, C. Hub, R. Fink, C. Wang, T. Schuettfort, C. R. McNeill, M. L. Chabinyc, H. Ade, *Nat. Mater.* **2012**, *11*, 536.
[51] B. A. Collins, E. Gann, *J. Polym. Sci.* **2021**, *60*, 1199.
[52] T. Ferron, M. Pope, B. A. Collins, *Phys. Rev. Lett.* **2017**, *119*, 167801.
[53] Z. Shen, J. Yu, G. Lu, K. Wu, Q. Wang, L. Bu, X. Liu, Y. Zhu, G. Lu, *Energy Environ. Sci.* **2023**, *16*, 2945.
[54] F. Babbe, N. Nicoara, H. Guthrey, N. Valle, O. R. Sanchez, D. Aureau, H. Elanzeery, D. Sharma, J. L. Virtuoso, J. N. Audinot, A. Zelenina, S. Gharabeiki, T. Wirtz, S. Siebentritt, P. J. Dale, S. Sadewasser, D. Colombara, *Adv. Energy Mater.* **2023**, *13*, 2204183.
[55] B. Lin, X. Zhou, H. Zhao, J. Yuan, K. Zhou, K. Chen, H. Wu, R. Guo, M. A. Scheel, A. Chumakov, S. V. Roth, Y. Mao, L. Wang, Z. Tang, P. Müller-Buschbaum, W. Ma, *Energy Environ. Sci.* **2020**, *13*, 2467.